

# A coupled flow-stress-damage model for groundwater outbursts from an underlying aquifer into mining excavations

T.H. Yang<sup>a</sup>, J. Liu<sup>b,\*</sup>, W.C. Zhu<sup>a</sup>, D Elsworth<sup>c</sup>, L.G. Tham<sup>d</sup>, C.A. Tang<sup>a</sup>

<sup>a</sup>Center for Rock Instability and Seismicity Research, Box 138, Northeastern University, Shenyang 110004, China

<sup>b</sup>School of Oil and Gas Engineering, The University of Western Australia, WA 6009, Australia

<sup>c</sup>Department of Energy and Geo-Environmental Engineering, Pennsylvania State University, Pennsylvania, PA, USA

<sup>d</sup>Department of Civil Engineering, The Hong Kong University, Hong Kong

Accepted 24 April 2006

Available online 7 July 2006

## Abstract

Uncontrolled groundwater outbursts from underlying limestone aquifers into mining excavations present a significant safety challenge for underground coal mining in China. Although these mining hazards have been known for decades, the mechanism for groundwater outbursts remains elusive. A fully coupled flow-stress-damage model is presented to simulate the progressive development of fractures and the associated groundwater flow under incremental loading conditions resulting from mining processes. The model is based on classical theories of porous media flow and damage mechanics and importantly links changes in permeability with the accumulation of damage in following the complete stress–strain process. This coupled flow-stress-damage model is applied to examine the influence of mining advance on the initiation, extension, and evolution of an outburst conduit as it develops adjacent to the mine panel. Fractures are shown to initiate both from the wings of the excavation in shear, and from the center of the floor span, in extension. The growth of the extensile fractures is stunted by the presence of a high stress abutment, but the wing fractures extend, with one fracture becoming dominant. As the dominant fracture develops into the underlying over-pressured zone, water pressures transmitted along the now-open conduit reduce effective stresses and develop rapid heave displacements within the floor. The result is a groundwater outburst. The modeling is tuned to the results of laboratory experiments and follows the evolution of a viable outburst path. Observations corroborate with field measurements of permeability pre- and post-mining and are strong indicators of the veracity of the approach.

© 2006 Elsevier Ltd. All rights reserved.

**Keywords:** Underground coal mining; Groundwater outbursts; Flow-stress-damage model; Permeability evolution; Rock failure

## 1. Introduction

In China, a number of coal deposits are located above karst aquifers which contain large volumes of water. Groundwater under high pressure can breach the underburden around active mine panels, and burst into active mining excavations. For the last few decades, catastrophic inrushes of groundwater have comprised a significant and safety challenge for underground coal mining in China [1,2]. The improving safety when mining above ubiquitous over-pressured karst aquifers is a common concern of both mine operators and researchers.

### 1.1. Statement of the problem

It is of vital importance to know when, where, and how groundwater outbursts develop during mining processes [2–5]. Rock is a heterogeneous geological material which contains natural weakness at various scales. When rock is subjected to mechanical loading, these pre-existing weaknesses can close, open, extend or induce new fractures, which can in turn change the structure of the rock and alter its fluid flow properties. Accordingly, when mining excavations are made, the re-distribution of the stress field leads to the initiation and growth of cracks, and potentially creates a highly permeable damage zone around these excavations. This damage zone creates a pathway for water flow, reduces effective stresses close to the excavation, which in turn may further extend and dilate fractures that

\*Corresponding author. Tel.: +61 8 6488 7205; fax: +61 8 6488 1964.  
E-mail address: [jishan@cyllene.uwa.edu.au](mailto:jishan@cyllene.uwa.edu.au) (J. Liu).

## Nomenclature

|          |  |
|----------|--|
| $D$      | damage variable (dimensionless)                                |
| $E$      | damaged Young's modulus (Pa)                                   |
| $E_0$    | undamaged Young's modulus (Pa)                                 |
| $f_c$    | uniaxial compressive strength (Pa)                             |
| $f_{cr}$ | residual uniaxial compressive strength (Pa)                    |
| $f_t$    | uniaxial tensile strength (Pa)                                 |
| $f_{tr}$ | residual uniaxial tensile strength (Pa)                        |
| $F_i$    | body force (N/m <sup>3</sup> )                                 |
| $G$      | shear modulus (Pa)   |
| $k$      | intrinsic permeability (m <sup>2</sup> )                       |
| $k_0$    | intrinsic permeability tensor at zero stress (m <sup>2</sup> ) |
| $m$      | homogeneity index (dimensionless)                              |
| $p$      | pore fluid pressure (Pa)                                       |
| $s$      | property of element (such as strength or elastic modulus)      |
| $s_0$    | mean of property of element                                    |
| $u_i$    | displacement vector of solid skeleton (m)                      |

## Greek symbols

|          |   |
|----------|---|
| $\alpha$ | pore-pressure coefficient (dimensionless) |
| $\beta$  | coupling coefficient (Pa <sup>-1</sup> )  |

|                                |   |
|--------------------------------|---|
| $\varepsilon_{ij}$             | total strain tensor (dimensionless)                 |
| $\varepsilon_{t0}$             | strain at the peak tensile stress (dimensionless)   |
| $\varepsilon_{tu}$             | ultimate tensile strain (dimensionless)             |
| $\phi$                         | internal friction angle (°)                         |
| $\eta$                         | residual strength coefficient (dimensionless)       |
| $\lambda$                      | Lamé's constants (Pa)                               |
| $\sigma_{ij}$                  | stress tensor (Pa)                                  |
| $\sigma'_{ij}$                 | effective stress tensor (Pa)                        |
| $\sigma_1, \sigma_2, \sigma_3$ | the first, second and third principal stresses (Pa) |
| $\sigma_{ii}$                  | average stress (Pa)                                 |
| $\xi$                          | permeability increase factor (dimensionless)        |

## Special symbols

|                           |  |
|---------------------------|--|
| $\nabla \cdot \mathbf{A}$ | divergence of a vector (= div $\mathbf{A}$ ) |
| $\nabla A$                | gradient of a scalar (= grad $A$ )           |
| $\nabla \mathbf{A}$       | gradient of a vector (= grad $\mathbf{A}$ )  |

comprise the damage zone. This reinforcing feedback may either self-arrest, or ultimately accelerate towards an inrush event. Understanding key interactions of this coupled flow-stress-damage behavior are a key component in mitigating the occurrence and effects of outbursts. Although this phenomenon has been known for decades, the contributing mechanisms remain elusive. This knowledge gap has limited our ability to address this crucial issue for safer mining, and defines the objective of this study.

### 1.2. Previous studies

A number of theoretical models [6–10] have been presented to analyze changes in rock mass permeability that result from excavation-induced deformations. These include relationships between deformations of floor strata and permeability [11] using coupled fluid flow and solid deformation, and have evolved to incorporate complex constitutive laws [3,4] capable of following the outburst process. These studies of fracture behavior and extent during double face mining above a confined aquifer [3,4] have been extended to examine retarded outburst along pre-existing faults [5]. These include consideration of fault extension and weakening [5], and stress redistribution and strata failure [2] which in turn promote permeability enhancement. These studies have variously used field observations [2–5], numerical modeling [3–5], and physical analogs [2]. Although these theoretical models and numerical investigations have contributed significantly to our scientific understanding of groundwater outbursts,

crucial questions of when, where and how these events may develop during mining remain unanswered.

Rock mass permeability is known to be strongly stress- and stress-history dependent. The growth of micro-cracks, together with the accumulation of inelastic strain, occurs in brittle rock when it is subjected to differential stress. As cracks grow, coalesce, and interconnect, permeability is significantly altered, and usually increases [12]. This behavior is a consequence of dilatancy and may endure to 80% of peak strength [13]. In many references [14–18], the permeability increase during the formation of compaction band is reported. Wang and Park [3] considered permeability enhancement the key mechanism promoting groundwater outburst in the floor. Therefore, it is crucial to consider changes in permeability that result from rock failure, especially in the strain softening regime of brittle failure. Combined ultrasonic and permeability measurements on rock salt [19] have illustrated the linkage between mechanical damage and transport properties in an analog to brittle failure—cumulative damage initiates dilatancy, that in turn enhances permeability. Changes in permeability that result from deviatoric loading of granite may be as large as two to three orders of magnitude [20]. Such changes have also been recorded adjacent to underground excavations in rock where changes in permeability result from the evolution of the damage zone [12,21].

Finite element, boundary element, finite difference, and discrete element methods, have all been applied to simulate the damage behavior of rocks or rock masses. Jeffrey [22] used a discrete crack model to study the hydraulic

fracturing process. Valko [23] used Kachanov's and a Perkins–Kern–Nordgren-type model to study cumulative damage and failure process of rock under increasing hydraulic pressure. Discrete element [24] and particulate mechanics [25] models have been used to follow permeability changes that result from fabric evolution in fractured rock masses, including application to dual permeability transport models [21]. Separate models for heat and fluid flow, and for mechanical deformation have been interfaced [26] to solve coupled thermal flow problems, in the disposal of radioactive wastes, but neglect fracture propagation and damage evolution [27] as a mode of permeability development. As a consequence, such models cannot explicitly represent flow-damage coupling mechanics during fracture initiation, propagation, and coalescence in stressed rocks.

### 1.3. About this study

In this study, a coupled flow-stress-damage (FSD) model [28] is presented that explicitly represents a relationship between stress, damage and permeability. Importantly, permeability evolves both with the growth of the existing fractures, and with the formation of new fractures, that result from the process of rock failure. This model is then applied to provide insights into where, when, and how, groundwater outbursts may occur, with particular reference to mining geometries at the Yangcun Colliery (Yanzhou Mine Group, eastern China). This is completed through explicit simulations of the evolving path of groundwater outburst as mining advances.

## 2. Model description

### 2.1. Basic assumptions

A model of coupled flow, stress and damage is proposed that incorporates the following:

- The rock mass is fully saturated, with fluid (water) flow in the deforming medium accommodated through Biot's theory of consolidation [29].
- Permeability varies with stress state under elastic deformation, and is controlled by damage accumulation as the element fails.
- The rock is brittle-elastic, with a defined residual strength, and the loading and unloading behavior described consistent with the tenets of elastic damage mechanics [30,31].
- An element is considered to have failed when stress reaches strength. In tension, this is when the defined tensile strength is reached. In shear, this is when the shear stress reaches that defined by the Mohr–Coulomb failure envelope [30,31].
- Mechanical properties are assumed locally heterogeneous (including Young's modulus, strength) and are

represented by the Weibull distribution,

$$\varphi = \frac{m}{s_0} \left( \frac{s}{s_0} \right)^{m-1} \exp \left[ - \left( \frac{s}{s_0} \right)^m \right], \quad (1)$$

- where  $s$  is the element property (strength or elastic modulus) distributed about the mean,  $s_0$ . The parameter  $m$  is a homogeneity index, which may be obtained from the statistical distribution of rock mass parameters. In previous papers (Zhu and Tang, 2004; Tang et al., 2000) the validation of using of Weibull distribution in describing the heterogeneity of rock had been given.

### 2.2. Coupled equations of flow and stress (FS model)

The mechanical constitutive behavior is coupled into a continuum model for coupled flow and deformation in saturated media through Biot's theory of consolidation [29]. Changes in permeability are accommodated by relating permeability magnitudes to effective stresses. The complete set of mechanical and flow equations for steady behavior are defined as:

*Equilibrium equation,*

$$\sigma_{ij,j} + F_i = 0 \quad (2)$$

*Strain–displacement relation,*

$$\varepsilon_{ij} = \frac{1}{2}(u_{i,j} + u_{j,i}) \quad (3)$$

*Constitutive equation,*

$$\sigma'_{ij} = \sigma_{ij} - \alpha p \delta_{ij} = \lambda \delta_{ij} \varepsilon_v + 2G \varepsilon_{ij} \quad (4)$$

*Seepage equation,*

$$k \nabla^2 p = 0, \quad (5)$$

where  $\sigma$  is the stress tensor,  $F_i$  is the component of the body force,  $\varepsilon$  is the strain tensor,  $u_i$  represents the displacement vector of the solid,  $p$  is the pore-fluid pressure,  $\alpha$  is the pore-fluid pressure coefficient,  $\lambda$  and  $G$  are Lamé's constants, and  $k$  is the intrinsic permeability. The above Eqs. (2)–(5) [29] are supplemented with an additional constraint to represent the effective stress-dependent permeability:

$$k(\sigma_{ii}, p) = \xi k_0 e^{-\beta(\sigma_{ii}/3 - \alpha p)}, \quad (6)$$

where  $k_0$  is the initial hydraulic conductivity,  $\sigma_{ii}/3$  is the average stress, and  $\beta$  is the coupling parameter that reflects the influence of stress on the coefficient of permeability. When  $\xi > 1$ , Eq. (6) represents an increase in permeability that is caused by damage. The value of  $\xi$  can be obtained from experiments [3,9,32–34].

The magnitude of the pore-fluid pressure coefficient,  $\alpha$ , is also a function of damage [35]. In this study, the pore-fluid pressure coefficient of a mesoscopic element is assigned as  $0 < \alpha < 1$  and  $\alpha = 1$  for undamaged and completely damaged states (cracked stage), respectively [34,35].

The above system of equations are solved via finite elements and implemented into the continuum code



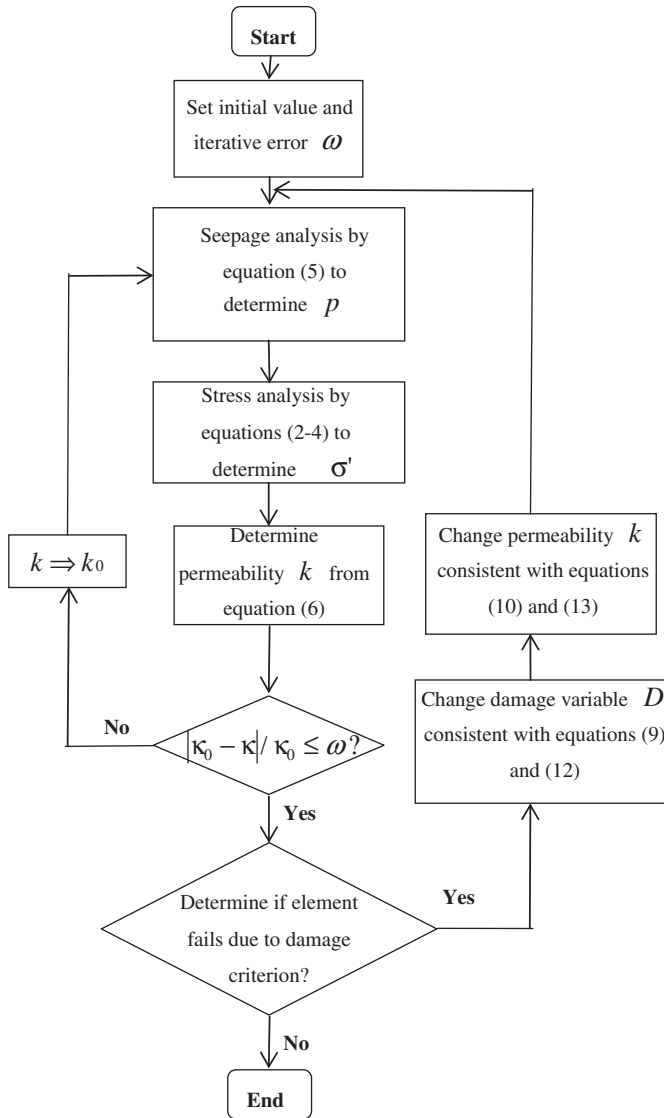


Fig. 2. The flow chart of RFPA<sup>2D</sup> program.

2.4. Numerical implementation of FSD model

This section describes the numerical implementation of the coupled FSD model, outlined in the previous sections, into the framework of this code. The solution steps are as follows (see Fig. 2):

- (1) initiate solution using a prescribed finite element mesh;
- (2) from flow boundary conditions, solve the seepage model for the distribution of fluid pressures (for an assumed permeability);
- (3) conduct an effective stress analysis to solve for the mechanical displacements;
- (4) reconcile coupling between stress and flow for displacements compatible with the effective stress field (FS model);
- (5) update permeabilities for the evolution of damage (FD model).

The model is finely discretized to accommodate local variations of material heterogeneity. During simulation, the model is loaded in a quasi-static fashion. At each loading increment, the seepage and stress equations are solved and the coupling analysis is performed. The stress field is then examined, and those elements that are stressed beyond the pre-defined strength threshold levels are assumed to be irreversibly damaged. The stiffness and strength of the damaged elements are reduced, and permeabilities are accordingly increased. The model, with associated new parameters, is then re-analyzed. The next load increment is added only when there are no more elements strained beyond the strength-threshold corresponding to the equilibrium stress field and a compatible strain field. The model iterates to follow the evolution of failure along a stress path, and in pseudo-time. The evolving state variables (stress, strain, fluid pressure) and material properties (modulus, permeability) overprinted on the initially heterogeneous field of strength and modulus [25], may be visualized to follow the progress of the outburst process.

3. A case study

The FSD model, as described above, is applied to evaluate the process of groundwater outburst in the Yangchun coal mine. The mine is located in Yan Zhou city, Shan Dong Province, eastern China, covers an area of 28.4 km<sup>2</sup>, with an annual production of 120 million tons. Extraction is by longwall mining, with a typical mining geometry illustrated in Fig. 3. The geologic profile comprises (Fig. 4) Quaternary (180 m) and Permian (50 m) strata overlaying, 160 m of Carboniferous mudstones and limestone that contain the coalbed. This in turn is underlain by 400–700 m of Ordovician limestone.

Mining occurs in the 2 m thick #17 coalbed located in the Carboniferous stratum, and separated by a 10–30 m aquiclude from three highly conductive limestone sub-units (#12, #13 and #14). These units are each 3–5 m thick, are individually separated by impermeable shale layers, but connected by a fault to the underlying Ordovician lime-

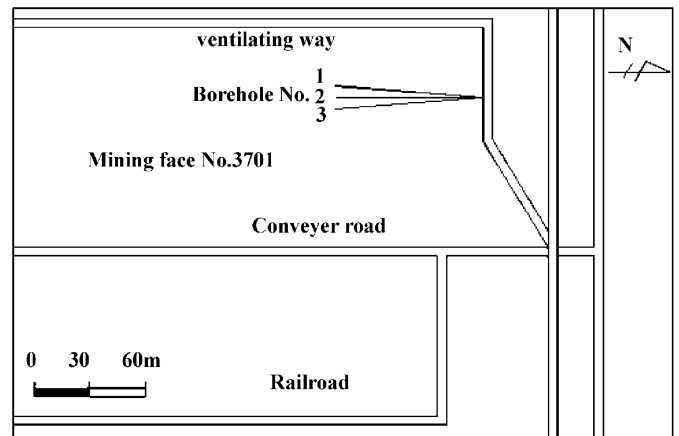


Fig. 3. Plan view of mining face No. 3701 in Yangchun coal mine.

stone. The in-situ flow capacity of these units is measured as 0.01–0.3 litre/s.m, with an ambient fluid pressure of 2 MPa. The massive Ordovician limestone is located 30–50 m underneath the coal seam with a flow capacity of 0.4–0.8 litre/s.m and hydraulic pressure of 3–5 MPa, and is the dominant aquifer implicated in groundwater outbursts.

Mining occurs directly above these confined aquifers, with the coal seam located at an average depth of 300 m. The Taiyuan limestone stratum, which lies 30–60 m below the coal seam, is a confined aquifer with hydraulic pressure up to 3–5 MPa. In the past few years, groundwater outbursts occurred frequently at the mining face, especially within the opening cut.

Although most observed groundwater outbursts are linked to the presence of faults, failures at Yangcun Colliery occur preferentially by the failure of the confining

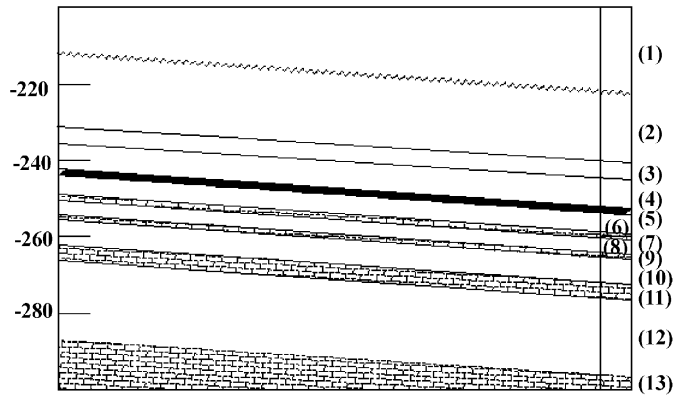


Fig. 4. Vertical section through the mining face (No. 3701) in the Yangchun coal mine: (1) Quaternary period stratum (2) sandy shale (3) limestone 10#, (4) mudstone, (5) coal seam #17, (6) mudstone, (7) limestone #12, (8) mudstone, (9) limestone #13, (10) mudstone, (11) limestone #14, (12) mudstone and (13) Ordovician limestone.

beds that represent an impervious barrier to flow. Since 1989, when the Yangcun colliery began operations, a total of 11 groundwater outbursts have been recorded. Investigations have found that these events were caused by the mining-induced failure of the impervious aquifers located below the #17 coal seam. Groundwater outbursts occur when a fracture zone forms that progressively links the high pressure aquifer with the coal seam. When the mining face advances 20–30 m from the opening, groundwater outbursts are most likely to occur as stress concentrations around the panel are exacerbated immediately before the first collapse of the main roof strata. In many cases, groundwater outbursts occur through the coal mine floor near the back of the mining face. Correspondingly, we apply the FSD model to evaluate the process of mining-induced groundwater outbursts with a focus on this specific location.

3.1. Numerical model

A model is assembled to incorporate the specific geological and geometric conditions detailed above (Figs. 3 and 4). As shown in Fig. 5, the simulation domain is 250 m long and 100 m high. It contains a total of 12 rock layers and the single embedded coal seam. The model includes a 60 m long floor stratum. Between the #17 coal seam and the Ordovician limestone, there are a total of 8 strata, among which the #12, #13, and #14 limestones are water bearing strata. Confining mudstone layers separate the water-bearing limestones.

The simulation domain is discretized into 150 × 375 elements for a total of 56250 elements with a uniform dimension of 2/3 m × 2/3 m. The bottom boundary of this model is constrained in the vertical direction, and both the left and the right boundaries are constrained in the

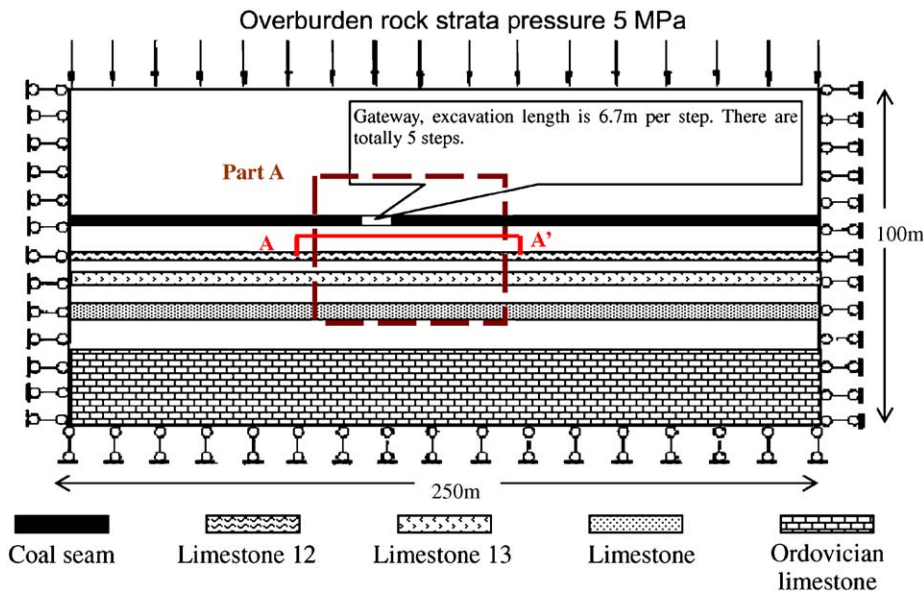


Fig. 5. Hydromechanical model of the double longwall mining geometry above the confined limestone aquifer.

horizontal direction. A pressure of 5 MPa is applied on the top boundary of the model to simulate gravitational loading of the overburden. A fluid pressure of 3.5 MPa is applied to the external boundary of the Ordovician limestone, and pressures of 0.8 (#12), 2.9 (#13), and 3.1 (#14) MPa are applied to the boundaries of the intervening limestone units, as measured in situ.

### 3.2. Determination of mechanical and hydraulic properties

In order to establish the strain–permeability relations for the numerical model, a series of laboratory tests were conducted on different rock samples. Samples were recovered from the mine floor strata. Rock cores with a total length of 40 m were collected in the unit underlying the #17 coal seam at a depth of 300 m, to sample the interbedded Carboniferous and Ordovician shales and limestones. The rock cores were cut into cylinders with a diameter of 54 mm and height of 55–80 mm, and coupled deformation permeability tests conducted in jacketed samples. Confining stresses of 4–6 MPa and pore fluid pressures of 3.8–5.8 MPa replicated in situ conditions. Tests were axial load controlled with axial stress  $\sigma_1$ , strain  $\epsilon_1$ , and pore pressure kept constant at each loading level. Permeability was measured by end-to-end flow tests by decreasing the pore pressure at the top platen to form a differential pressure between the two ends; the axial stress, strain and permeability were recorded over a time interval of 20 s.

Fig. 6 shows the strain–permeability curves recovered for different strata under conditions of triaxial compression. In both cases, permeability increases with an increase in strain. The permeability of the mudstone rises monotonically with the application of load, peaks, and then decreases in the post-peak stress regime. The mudstone has a high residual strength and exhibits only mild strain-

softening behavior. Conversely, the initially low permeability limestone sustains no change in permeability until strains are of the order of 0.005. Subsequently, permeability increases sharply before again ultimately decreasing in the post-peak regime. The limestone is more strongly strain softening with a pronounced residual strength.

These experimental results provide the basis to determine the reduction coefficient for permeability in the pre-failure region and the enhancement coefficient for permeability in the post-failure region, for component rocks. These coefficients are essential for the numerical simulation.

The inelastic strain-recovery method was used to measure the in situ stress located at the –273 m level of the Yangcun Colliery. Data from the measurements indicated that gravitational loading dominates the in situ stress field with a slight addition from the tectonic stress field. The direction of the maximum principal stress is approximately vertical with a magnitude of 7.8 MPa. The intermediate and minimum principal stresses are horizontal with magnitudes 6.20 and 5.23 MPa, respectively. Table 1 lists the averaged values of the mechanical properties of rock mass recovered from various in situ experiments. Based on the full data set, the corresponding homogeneity index for the mechanical parameters (Young's modulus, strength)  $m$  is set as 10. The post-failure values of the permeability adjustment factor  $\xi$ , and the residual strength coefficient  $\eta$ , are defined as 50 and 0.1, respectively.

### 3.3. Simulation of groundwater outburst processes

In the following, we follow the progressive evolution of the outburst path during a six-step mining sequence with the advance increment of 6.7 m/step. As mining advances, rock failure occurs in the surrounding rocks. The failure initiates at isolated locations that ultimately coalesce to form a continuous failure zone. We use the evolution of the

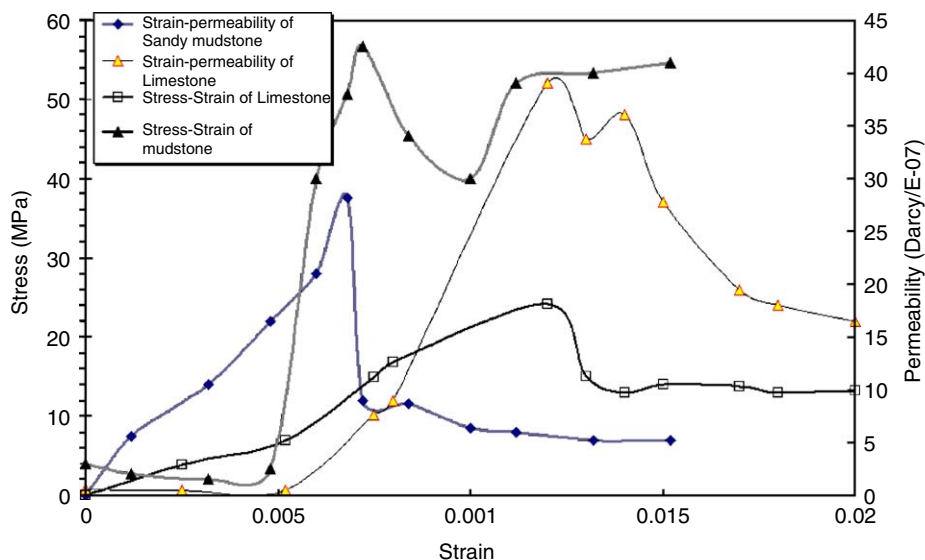


Fig. 6. Evolution of permeability with strain for sandy mudstones and limestone under triaxial compression.

Table 1  
Rock mass mechanics parameters

| Rockmass type        | Thickness (m) | Young's modulus $E_0$ (MPa) | Compressive strength $f_c$ (MPa) | Tensile strength $f_t$ (MPa) | Internal cohesive angle $\phi$ (deg) | Poisson's ratio $\mu$ | Weight ( $\text{kg/m}^3$ ) $\rho$ | Hydraulic conductivity $k_0$ (m/d) | Pore water pressure coefficient $\alpha$ |
|----------------------|---------------|-----------------------------|----------------------------------|------------------------------|--------------------------------------|-----------------------|-----------------------------------|------------------------------------|--|
| Overburden layer     | 10            | 2000                        | 2                                | 0.1                          | 30                                   | 0.25                  | 1800                              | 0.14                               | 0.1                                      |
| Sandy shale          | 17            | 3000                        | 7                                | 0.35                         | 37                                   | 0.2                   | 2500                              | 0.14                               | 0.1                                      |
| Limestone #10        | 6             | 8800                        | 6.4                              | 0.32                         | 40                                   | 0.2                   | 2800                              | 11.6                               | 0.1                                      |
| Mudstone             | 5             | 1640                        | 5.2                              | 0.26                         | 30                                   | 0.28                  | 2500                              | 0.14                               | 0.01                                     |
| Coal seam 17         | 2             | 1340                        | 5                                | 0.25                         | 30                                   | 0.31                  | 2100                              | 0.14                               | 0.01                                     |
| Mudstone             | 7             | 1640                        | 5                                | 0.25                         | 30                                   | 0.28                  | 2540                              | 0.14                               | 0.01                                     |
| Limestone #12        | 3             | 9710                        | 8                                | 0.4                          | 39                                   | 0.21                  | 2500                              | 87.5                               | 1  |
| Mudstone             | 2             | 1810                        | 5                                | 0.25                         | 34.5                                 | 0.29                  | 2500                              | 0.14                               | 0.01                                     |
| Limestone #13        | 4             | 9710                        | 8                                | 0.4                          | 29                                   | 0.2                   | 2500                              | 87.5                               | 1  |
| Mudstone             | 5             | 1640                        | 5                                | 0.25                         | 30                                   | 0.28                  | 2500                              | 0.14                               | 0.01                                     |
| Limestone #14        | 5             | 8870                        | 8                                | 0.4                          | 36                                   | 0.21                  | 2500                              | 87.5                               | 1  |
| Mudstone             | 15            | 1640                        | 5                                | 0.25                         | 30                                   | 0.29                  | 2500                              | 0.14                               | 0.01                                     |
| Ordovician limestone | 20            | 10000                       | 10                               | 0.5                          | 30                                   | 0.2                   | 2500                              | 87.5                               | 1  |

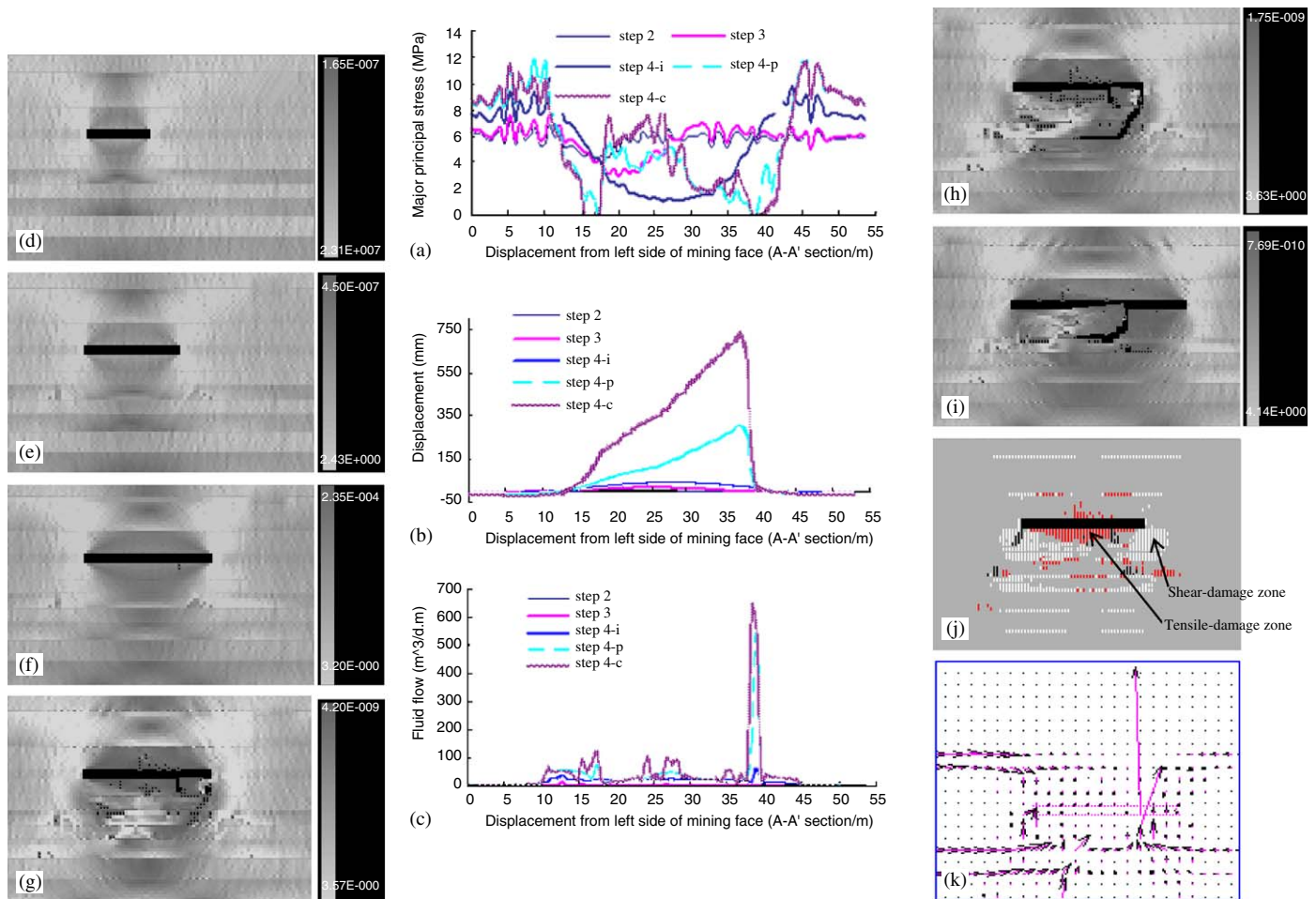


Fig. 7. Numerical evolutions of stress, displacement, and flow rate during the progressive formation of a continuous groundwater outburst path linking the mining face to the aquifers. (a) Maximum principal stress distribution in the mine floor; (b) the vertical displacement in mine floor; (c) the vertical fluid flow in mine floor; (d) shear stress in mining step 2; (e) shear stress in mining step 3; (f) shear stress in mining step 4-i; (g) shear stress in mining step 4-p; (h) shear stress in mining step 4-c; (i) shear stress in mining step 5; (j) damage distribution in mining step 4-p; (k) flow vector in step 4-c.

damage parameter (operating on modulus), or the failure shear stress, as an index to visualize the evolution of failure zones. This failure zone is the potential path for ground-

water in developing an outburst structure. These processes were simulated explicitly as shown in Figs. 7(a)–(h). Fig. 7(a) shows the stress distributions that develop within

the excavation floor; Fig. 7(b) shows the vertical displacement along the excavation floor; Fig. 7(c) shows the flow rate along the excavation floor; and Figs. 7(d)–(k) show the distribution of shear stresses (crack evolution), damage zone and fluid flow field at different simulation steps.

In these figures the gray level represents the magnitude of the shear stress. These graphical visualizations illustrate clearly the initiation (Step 4-i), propagation (Step 4-p), and the coalescence (Step 4-c) of features comprising the outburst path. These processes are explained according to the mining steps as follows.

With the first excavation to 6.7 m from the left boundary, no failure initiates. The second cut concentrates compressive stresses around the opening and within the coal rib. The maximum compressive stress in these areas is 6.9 MPa, as shown in Figs. 7(a) and (d). Stress is released in the middle of the panel floor where the maximum compressive stress is 4.1 MPa, shear damage occurs near the corner of the coal rib but around the goaf the damaged zone is small. Therefore, the floor of the excavation is still stable even though the maximum vertical displacement at the center of the excavation floor has reached 10 mm, as shown in Fig. 7(a).

When the mining face extends to 20.1 m in the third cut, the compressive stress in the middle of the floor is 3.4 MPa, as shown in Figs. 7(a) and (d), and the failure zone below the two coal ribs grows larger. Tensile failure occurs near the water-bearing #12 limestone although no groundwater inrush yet occurs. The underlying impermeable layer remains intact despite a vertical displacement of 16 mm in the excavation floor, as shown in Fig. 7(b).

When the mining face extends to 26.8 m in the fourth cut, the maximum compressive stress at the coal rib is 12 MPa, and the compressive stress in the middle of the excavation floor is 1.3 MPa, as shown in Fig. 7(a). The stresses around the excavation adjust continuously before the initiation of the groundwater outburst path. Under the action of pore pressure and ground stress, the impermeable layer above #12 limestone heaves and tensile damage accumulates in the center, as shown in Fig. 7(g). A tensile-shear failure zone also develops at the coal ribs as shown in Fig. 7(j). Fig. 7(j) gives the damage distribution at step 4-p (Fig. 7(g)), where different colors are used to denote different damage modes: red is for the elements that are damaged in tension at current step; white is for the elements that are damaged in shear at current step; and black is for the elements that are damaged at previous steps. There is very few elements damage before and after step 40-p, therefore, only the damage distribution at step 4-p is shown.

This zone penetrates into #12 limestone and results in the groundwater outburst as shown in Fig. 7(h). After the outburst, dramatic changes in stress occur in the neighborhood of the main fractures connecting to the opening, and these changes affect directly the growth of the fractures that develop downwards to #13 and #14 limestones, as shown in Fig. 7(h). The compressive stress in the floor of the coal rib reduces to nearly zero, as shown in Fig. 7(a),

while the compressive stress in the middle of the excavation floor increases to a magnitude of 4.4 MPa, as shown in Fig. 7(a). This is due to fracturing and heaving in the impermeable floor under the effect of hydraulic pressure, as shown in Fig. 7(g). The maximum displacement at the location of groundwater outburst is about 700 mm as shown in Fig. 7(b), and the flow rate is  $\sim 650 \text{ m}^3/\text{d.m}$ , as shown in Fig. 7(c).

When the mining face advances to 33.5 m in the fifth mining sequence, the pore pressure decreases gradually, and therefore, the path of the outburst does not extend further, as shown in Fig. 7(i).

These explicit simulations show that the fracture within the excavation floor develops downwards at the two ends of the mining face as shown in Fig. 7(j), and the fracture within the impermeable layer above the limestone results in only a small contribution to the overall breakthrough. Of the fractures at each end of the mining face, only one becomes dominant, and ultimately grows suddenly into the excavation floor. This sudden growth leads to the development of a through-going fracture which hydraulically links #12 and #13 limestones, by transecting the impermeable intervening strata. This precipitates an outburst, but only taps the two smaller limestone aquifers, limiting the danger posed by the inrush. Only if the smaller limestone units are connected to the Ordovician limestone will the resulting inrush be more substantial.

### 3.4. Comparison with in situ hydraulic experiments

In order to determine the potential location and depth of floor failure, pre- and post-mining water injection tests were conducted in three bore holes, at locations shown in Fig. 3. Tests were for constant water head, and use observed changes in flow rate as a direct index of change in permeability, pre- and post-mining. The test results are shown in Fig. 8, indicating low pre-mining hydraulic conductivities, and confirming that permeability increased as a consequence of mining. This conclusion is consistent with the results of the modeling, except no outburst occurred.

## 4. Conclusions

A fully coupled flow-stress-damage model is presented to follow the evolution sequence and path of over-pressured groundwater water outbursts into mined panels. The model accommodates the interaction of stress and fluid effects through a continuum theory based on Biot poroelasticity. Critical features of the analysis are a linkage between the evolution of rock damage and related changes in permeability. Damage is represented by a linear mapping of elastic modulus, indexed against failure criteria in both extension and shear. Changes in permeability that occur as a consequence of damage are mapped by a linear factor tuned to experimental results for permeability enhancement in intact rocks.

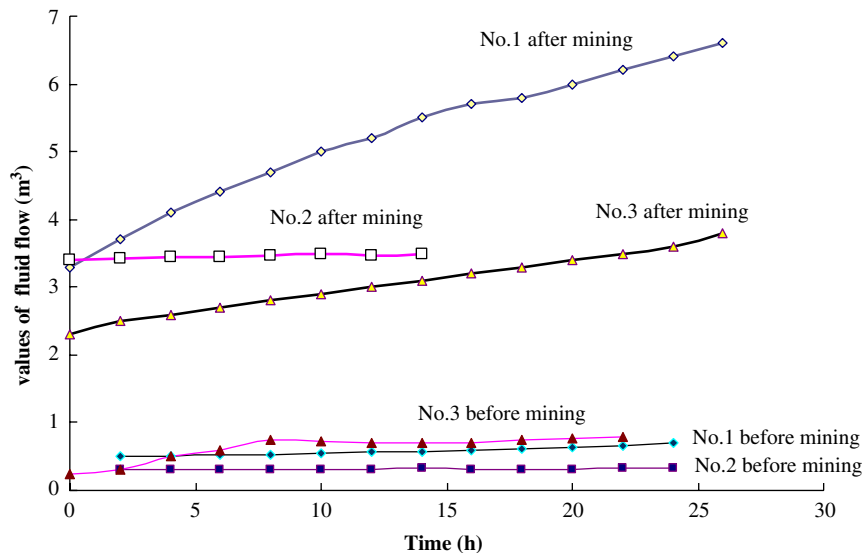


Fig. 8. Observed changes in fluid flow rate at boreholes #1, #2 and #3 both pre- and post-mining.

Apparent from the results are the generation of through-going fractures that link underlying over-pressured regions with the mine panel. Fractures are shown to initiate both from the wings of the excavation in shear, and from the center of the floor span, in extension. The growth of the extensile fractures is stunted by the presence of a higher stress abutment in the floor, but the wing fractures extend, with one fracture becoming dominant. As the dominant fracture develops into the underlying over-pressured zone, water pressures transmitted along the now-open conduit reduce effective stresses and develop rapid heave displacements within the floor. The result is a groundwater outburst.

The modeling is tuned to the results of laboratory experiments, follows the evolution of a viable outburst path, and is corroborated with field measurements of permeability pre- and post-mining. Combined, these observations are strong indicators of the veracity of the approach. The explicit nature of the simulations makes RFPA<sup>2D</sup> a potentially powerful tool for understanding the mechanisms of groundwater outbursts, and in the design of strategies to mitigate them.

### Acknowledgments

This work presented in this paper is the result of partial support by the National Natural Science Foundation (Grant Nos. 50490274, 50204003, 50134040, 50504005 and 50174013) of China, and the ARC LX0451750. The authors wish to thank Professor Q Y Feng for providing the in situ test data.

### References

[1] Jiuchuan W, Baiying L. Security evaluation of coal mining above the confined aquifers. *Coal Geol Explorat* 2000;8:57–9 [in Chinese].

- [2] Jincui Z, Baohong S. A Coal mining under aquifers in China: a case study. *Int J Rock Mech Min Sci* 2004;41:629–39.
- [3] Wang JA, Park HD. Fluid permeability of sedimentary rocks in a complete stress-strain process. *Eng Geol* 2002;63:291–300.
- [4] Wang JA, Park HD. Coal mining above a confined aquifer. *Int J Rock Mech Min Sci* 2003;40:537–55.
- [5] Wu Q, Wang M, Wu X. Investigations of groundwater bursting into coal mine seam floors from fault zones. *Int J Rock Mech Min Sci* 2004;41:557–71.
- [6] Bear J, Tsang CF, Marsily D. *Flow and contaminant transport in fractured rock*. New York: Academic Press; 1993.
- [7] Zhang L, Franklin JA. Prediction of water flow into rock tunnels: an analytical solution assuming a hydraulic conductivity gradient. *Int Rock Mech Sci Geomech Abstr* 1993(1):37–46.
- [8] Minggao Q, Xiexing M, Jianlin X. Theoretical study of key stratum in ground control. *J China Coal Soc* 1996;21(3):225–30 [in Chinese].
- [9] Zhang JC. Stress-dependent permeability variation and mine subsidence. In: Girard, Liebman, Breeds, Doe, editors. *Pacific Rocks 2000*. Rotterdam: Balkema; 2000. p. 811–6.
- [10] Lianguo W, Yang S. A catastrophic model of water-inrush from coal floor. *J Eng Geol* 2000;8(2):160–3 [in Chinese].
- [11] Dong Y, Yangsheng Z. Numerical simulation of solid-fluid coupling function of fracture media. *J China Coal Soc* 1998;23(1):37–41 [in Chinese].
- [12] Souley M, Homand F, Pepa S, Hoxha D. Damage-induced permeability changes in granite: a case example at the URL in Canada. *Int J Rock Mech Min Sci* 2001;38:297–310.
- [13] Zoback MD, Byerlee JD. The effect of microcracks dilatancy on the permeability of Westerly granite. *J Geophys Res* 1975;80:752–5.
- [14] Holcomb DJ, Olsson WA. Compaction localization and fluid flow. *J Geophys Res* 2003;108:2290.
- [15] Olsson WA, Holcomb DJ. Compaction localization in porous rock. *Geophys Res Lett* 2000;27:3537–40.
- [16] Wong TF, David C, Zhu WL. The transition from brittle faulting to cataclastic flow in porous sandstones: Mechanical deformation. *J Geophys Res* 1997;102:3009–25.
- [17] Wong TF, Baud P, Klein E. Localized failure modes in a compactant porous rock. *Geophys Res Lett* 2001;28:2521–4.
- [18] Yuan SC, Harrison JP. Numerical modeling of progressive damage and associated fluid flow using a hydro-mechanical local degradation approach. *Int J Rock Mech Min Sci* 2004;41:417–8.

- [19] Schulze O, Popp T, Kern H. Development of damage and permeability in deforming rock salt. *Eng Geol* 2001;61:163–80.
- [20] Oda MT, Takemura A, Aoki T. Damage growth and permeability change in triaxial compression tests of Inada granite. *Mech Mater* 2002;34:313–31.
- [21] Xing Z, Sanderson DJ, Barker JA. Numerical study of fluid flow of deforming fractured rocks using dual permeability model. *Geophys J Int* 2002;151:452–68.
- [22] Jeffrey RG, Mills KW. Hydraulic fracturing applied to inducing longwall coal mine goaf falls. In: Girard, Liebman, Breeds, Doe, editors. *Pacific Rocks 2000*. Rotterdam: Balkema; 2002. p. 423–30.
- [23] Valko P, Economides MJ. Propagation of hydraulically induced fractures—a continuum damage mechanics approach. *Int. J. Rock Mech Min Sci Geomech Abstracts* 1994;31(3):221–9.
- [24] Thallak S, Rothenburg L, Dusseault M. Simulation of multiple hydraulic fractures in a discrete element system. In: *Rock mechanics as a multidisciplinary science* Roegiers M., editors. Rotterdam: Balkema; Proceedings of the 32nd US symposium, 1991, p. 271–280.
- [25] Li L, Holt RM. Simulation of flow in sandstone with fluid coupled particle model. In: Elsworth, Tinucci, Heasley, editors. *Rock mechanics in the national interest*. Swets Zeitinger Lisse; 2001. p. 165–72.
- [26] Rutqvist J, Tsang CF. Analysis of thermal-hydrologic-mechanical behavior near an emplacement drift at Yucca Mountain. *J Contam Hydrol* 2003;62–63:637–52.
- [27] Mahnken R, Kohlmeier M. Finite element simulation for rock salt with dilatancy boundary coupled to fluid permeation. *Comput Methods Appl Eng* 2001;190:4259–78.
- [28] Tang CA, Tham LG, Lee PKK, Yang TH, Li LC. Coupled analysis of flow, stress and damage (FSD) in rock failure. *Int J Rock Mech Min Sci* 2002;39:477–89.
- [29] Biot MA. General theory of three-dimensional consolidation. *J Appl Phys* 1941;12:155–64.
- [30] Tang CA, Liu H, Lee PKK, Tsui Y, Tham LG. Numerical studies of the influence of microstructure on rock failure in uniaxial compression Part I: effect of heterogeneity. *Int J Rock Mech Min Sci* 2000;37:555–69.
- [31] Zhu WC, Tang CA. Numerical simulation on shear fracture process of concrete using mesoscopic mechanical model. *Construct Building Mater* 2002;16(8):453–63.
- [32] Li S P, Wu D X. Effect of confining pressure, pore pressure and specimen dimension on permeability of Yin Zhuang sandstone. *Int J Rock Mech Min Sci* 1997;34(3/4):435–41.
- [33] Li SP, Li YS, Wu ZY. Permeability-strain equations corresponding to the complete stress-strain path of Yin Zhuang sandstone. *Int J Rock Mech Min Sci Geomech Abstr* 1994;31(4):383–91.
- [34] Yang TH, Tham LG, Tang CA, Liang ZZ. Influence of heterogeneity of mechanical properties on hydraulic fracturing in permeable rocks. *Rock Mech Rock Eng* 2004;37(4):251–75.
- [35] Bernabe Y. The effective pressure law for permeability in Chelmsford granite and barre granite. *Int J Rock Mech Min Sci Geomech Abstr* 1986;23(3):267–75.